

Coherent Nuclear and Electronic Dynamics in Primary Charge Separation in Photosynthetic Reaction Centers: A Redfield Theory Approach

Vladimir I. Novoderezhkin,[†] Andrey G. Yakovlev,[†] Rienk van Grondelle,^{*,‡} and Vladimir A. Shuvalov[†]

A. N. Belozersky Institute of Physico-Chemical Biology, Moscow State University, Leninskie Gory, 119992, Moscow, Russia, and Department of Biophysics and Physics of Complex Systems, Faculty of Sciences, Vrije Universiteit, De Boelelaan 1081, 1081 HV Amsterdam, The Netherlands

Received: November 3, 2003; In Final Form: February 19, 2004

Primary charge separation dynamics is modeled in the pheophytin-modified *Rhodobacter sphaeroides* R-26 reaction center (RC). To explain the observed spectral evolution, it is assumed that the process is coupled to coherent nuclear motion. A density matrix equation with the Redfield relaxation superoperator is used for simulation of the electron-vibrational dynamics and its spectral signatures. The model includes two diabatic states, i.e., an excited state P^* of the primary donor (i.e., special pair, P), and a charge-transfer state (P^+B^- , which is the primary photoproduct in the pheophytin-modified RC). The strong coupling of these states with two collective nuclear modes is supposed. The mixing of diabatic states (with different displacements along each of the two nuclear coordinates) results in a complicated potential surface that determines the dynamics of the excited-state wave packet. The coupled nuclear and charge-transfer dynamics is calculated in the basis of vibronic eigenstates obtained by numerical diagonalization of the electron-vibrational Hamiltonian. The third-order nonlinear response associated with excited-state dynamics is calculated, including the $P^* \rightarrow P$ stimulated emission (SE) and the $P^+B^- \rightarrow P^+(B^-)^*$ excited-state absorption (ESA). The model allowed us to obtain a quantitative fit of the experimental kinetics of the SE near 900–950 nm and the ESA in the 1020-nm region of the pheophytin-modified *Rhodobacter sphaeroides* R-26 RC (Yakovlev, A. G.; Shkuropatov, A. Ya.; Shuvalov, V. A. *FEBS Lett.* **2000**, 466, 209). By use of the parameters adjusted from the fit, we have obtained a direct visualization of the electron-vibrational wave packet evolution, including the surface-crossing dynamics superimposed with oscillatory motion along two reaction coordinates in the P^* and P^+B^- states. It is concluded that nonequilibrated vibrational modes involved in electron-transfer play an important role in photoproduct formation in bacterial RC. We found that the specific configuration of two vibrational coordinates (obtained from the modeling) determines high efficiency of charge separation both for coherent and noncoherent excitation.

Introduction

Photosynthetic reaction centers (RCs) are very efficient systems for the conversion of electronic excitations into the free energy of charge-separated states.^{1,2} It is well established that the primary steps of electron transfer in RC are coupled to collective nuclear motions (intramolecular, intermolecular, protein) of the chromophore–protein complex. In the conventional theories of electron transfer, these nuclear motions are supposed to be thermally equilibrated (see, for review, refs 3 and 4). However, recent time-resolved spectroscopic studies have shown that strong coherent nuclear motions occur on the time scale of electron transfer in RC (see, for review, ref 5 and references therein). An adequate interpretation of the experimentally observed nonlinear response should include the effects of long-lived vibrational coherence. While a general physical approach to this problem was developed,⁶ all applications of the theory were so far restricted to rather simplified models. Analyses of the primary charge separation dynamics coupled to coherent nuclear motion were performed using the Liouville

equation,⁷ dispersed polaron model,⁸ and Langevin equation.⁹ These approaches allowed a qualitative explanation of a time-dependent (oscillating) probability of photoproduct formation, but they do not include details needed to visualize the whole electron-vibrational dynamics and to explain its spectral signatures at quantitative level.

In this paper, we use the density matrix equation with the Redfield relaxation superoperator in order to obtain a self-consistent and quantitative explanation of the nonlinear spectral response of the RC (including the oscillatory features in the primary donor and photoproduct bands). We use the density matrix in the basis of the ground, single-, and double-excited electron-vibrational manifolds to fit the transient absorption (TA) kinetics and visualize the dynamics of the excited-state vibrational wave packet along two reaction coordinates.

Experimental Studies of Bacterial RCs. Femtosecond pump–probe studies showed that the lowest excited state of the special pair (P^*) is coupled to a low-frequency vibrational mode, which represents collective nuclear motions.^{10–17} Earlier studies of the RCs of the so-called D_{LL} mutant of *Rhodobacter (Rb.) capsulatus* (in which electron transfer is blocked) showed that the low-frequency ($<150\text{ cm}^{-1}$) nuclear motions are coherent on the time scale of electron transfer in functional

* To whom correspondence may be addressed. E-mail: rienk@nat.vu.nl. Fax: +31-20-4447999.

[†] Moscow State University.

[‡] Vrije Universiteit.

RCs.¹⁰ The 30-fs resolution studies of membranes of the antenna-deficient RC01 mutant of *Rb. sphaeroides* containing wild-type RCs revealed strong oscillations in the stimulated emission (SE) from the (P*)₋ state and very weak oscillations in the photobleaching (PB) of the ground-state absorption at 10 K.¹¹ A fit of these kinetics using damped sinusoidal functions $\sum \exp(-\gamma_i t) \sin(\Omega_i t + \varphi_i)$ indicated a relatively fast decaying 122-cm⁻¹ mode ($\gamma^{-1} \approx 200$ fs) and more long lived 92- and 153-cm⁻¹ modes ($\gamma^{-1} > 500$ fs). The Fourier transform (FT) spectrum showed that also the range of <35 cm⁻¹ has significant vibrational strength. The observed oscillations have opposite phases on the blue and red side of the SE band and disappear in the middle of the band with the corresponding phase jump. At room temperature, oscillations are discernible during 1–1.5 ps after excitation.¹² The corresponding FT spectra have main components at 30 and 145 cm⁻¹ (probably a congestion of the 122- and 153-cm⁻¹ peaks observed at 10 K) with additional minor peaks at 84 and 192 cm⁻¹. By use of shorter pulses (12 fs), high-frequency oscillations at 560, 730, and 1160 cm⁻¹ were obtained for the *Rb. sphaeroides* R-26 RCs at room temperature together with the low-frequency 140-cm⁻¹ mode.¹⁷ In this experiment, oscillations were observed in the SE as well as in the excited-state absorption (ESA) of (P*)₋.

Coherent nuclear motion detected as oscillations in the SE of the lowest exciton state (P*)₋ can be also activated if (P*)₋ is populated from the higher exciton state (P*)₊. Excitation of (P*)₊ at 820 nm and excitation of (P*)₋ at 880 nm (for *Rb. sphaeroides* R-26 RCs at 15K) resulted in very similar kinetics in the SE region of (P*)₋.¹³ This means that exciton relaxation between levels separated by 600–700 cm⁻¹ does not influence the shape and phase of these coherent nuclear motions. Under broad-band excitation, it was possible to create a vibrational coherence together with the coherence between exciton states (P*)₊ and (P*)₋.¹⁷ The coherent motion of the exciton wave packet resulted in oscillations of the anisotropy with a frequency of 593 cm⁻¹ (which is close to the exciton splitting) and damping constant of 35 fs. After thermalization of the exciton states with a time constant of 60 fs, the kinetics were determined by the coherent motion of the vibrational wave packet in the (P*)₋ state. Because of the broad-band excitation, this wave packet contained high-frequency modes.¹⁷

Excitation of the special pair P is also accompanied by oscillations in the B-band region (around 800 nm).^{14,16,18} One possible explanation is that these oscillations are due to the electrochromic shift of the B-band induced by oscillating charges in the P⁺H⁻ state or by a coherent component in the dynamics of the P⁺H⁻ state population.^{14,19} Alternatively, a two-step coherent electron transfer was suggested including coherent formation of the B⁻ state.^{16,18} The data suggested that different vibrational modes have a different coupling to electron transfer. Interpretation of the data is complicated because the TA in the 800-nm region includes contributions from ESA of the P* state and shifts and bleachings of the B-band in the P*, P⁺B⁻, and P⁺H⁻ states.¹⁹

Direct observation of coherent formation of the P⁺B⁻ state is possible via measuring the TA around 1020 nm of a band originating from the BChl anion absorption.^{20–24} The first experiments²⁰ performed for wild-type *Rb. sphaeroides* R-26.1 RC showed oscillations in the SE region of the P* band (920–990 nm) and in the P⁺B⁻ band absorption (990–1050 nm with a maximum at 1020 nm) with the main frequency of 135 cm⁻¹ together with a weak low-frequency (40 cm⁻¹) mode. The low-frequency (40 cm⁻¹) oscillations were not stronger in the 1020-nm region, so that this mode was supposed to be not connected

with electron transfer (in contrast to the suggestion of refs 16 and 18). The frequencies and phases of the high-frequency (135 cm⁻¹) oscillations persisted through the whole 920–1100-nm spectral range, suggesting that they originated from the P* wave-packet motion (i.e., from the long wavelength tail of the SE near 1020 nm). Notice that relatively long laser pulses (60–100 fs) were used in this experiment, thus reducing the amplitude of the oscillations. No evidence for coherent motion in the product (P⁺B⁻) state was found, which was explained by fast vibrational equilibration on the P⁺B⁻ potential energy surface.

In contrast to these earlier studies, the latest measurements of native and pheophytin-modified *Rb. sphaeroides* R-26 RCs showed a wave-packet-like motion both in the SE region of the primary donor P* (900–950 nm) and in the absorption band of primary photoproduct P⁺B⁻ (around 1020 nm).^{21–23} Analysis of the whole spectral evolution (instead of the analysis of the kinetics in ref 20) allowed one to separate the ESA (P⁺B⁻ absorption) and the SE components. Both these components have pronounced oscillatory features with remarkable differences between the phases and FT amplitudes of their oscillatory patterns. Thus, the FT spectra of the SE P* and ESA P⁺B⁻ components contain two modes (30 and 130 cm⁻¹), with the low-frequency 30-cm⁻¹ mode significantly increased in the photoproduct oscillatory pattern. It is important that the SE P* and ESA P⁺B⁻ components near 1020 nm oscillate with opposite phases so that the ESA oscillations in the 1020-nm kinetics are hidden under the more intense oscillations from the tail of the SE P* band. This is why the coherence in the product (P⁺B⁻) state was not found in earlier experiments.²⁰ More detailed studies showed the presence of higher harmonics of the 30-cm⁻¹ mode that was ascribed to rotation of the H₂O molecule located between the P and B_A cofactors.²⁴ This conclusion was further corroborated by the frequency shift of this mode observed in the D₂O samples.²⁴ Observation of the oscillatory components in the H-band (760 nm) suggested that the 30-cm⁻¹ mode (enhanced in the P⁺B⁻ state) results in coherent P⁺H⁻ state formation.²³ Involvement of the 30-cm⁻¹ mode in the coherent dynamics of the P⁺H⁻ state formation was also suggested by analysis of the wavelength-dependent amplitudes and phases of the low-frequency (30 cm⁻¹) oscillations in the B-band.¹⁹

The experimental data obtained by the pump–probe, resonance Raman, and hole-burning studies of the RCs is summarized in Table 1.

Theoretical Modeling. The pump–probe oscillations in the P* band were modeled assuming a single electronic transition coupled to one or two vibrational modes.^{25–27} In the theories of Gu et al.²⁵ and Lin et al.,²⁶ the master equation for vibrational populations was used, and a simple exponential decay of the vibrational coherences was assumed. Leegwater²⁷ used a more general approach, including the processes of the vibrational coherence transfer via relaxation. Vibrational dynamics within the P* band was described by the Redfield theory in the secular approximation.

Vibrational dynamics within the primary donor (P*) and primary photoproduct (P⁺B⁻ or P⁺H⁻) bands coupled to the P* → P⁺B⁻ electron transfer was studied by Jean et al.^{7,28,29} using the Redfield theory and supposing a single nuclear mode coupled to the two electronic states. The time-dependent reaction coordinate together with the corresponding population dynamics of the initially excited P* state was calculated. Oscillatory features of the emission decay were also calculated (using some

TABLE 1: Parameters of Vibrational Modes Coupled to Electronic Excitations in the RCs^a

species	T, K	pump/probe, fs	λ probe, nm	main (minor) frequencies, cm ⁻¹	ref
<i>Rb. sphaeroides</i> RC01	10	30/30	938	15 69 92 122 153 191 329	11
<i>Rb. sphaeroides</i> RC01	15	30/15	900–960	70 94 125 156 195 335	14
<i>Rb. sphaeroides</i> RC01	300	30/30	938	84 145 192	12
		100/30	938	30	
<i>Rb. sphaeroides</i> R-26	300	12/12	930	140 560 730 1160	17
<i>Rb. sphaeroides</i>	300	RR		34 71 95 128 187 204 332 484 564 585 684 730 899 1163	33
<i>Rps. viridis</i> prereduced H _A	1.7	HB		31 73 110 147 175 205	34
<i>Rb. sphaeroides</i> R-26 BChl _B -modified	300	30/30	890	9 27 42 84 124	16
			805	10 32 83 133	
<i>Rb. sphaeroides</i> R-26 YM210W mutant	300	30/30	890	10 20 40 75 127	16
			805	1227 81 130	
<i>Rb. sphaeroides</i> R-26.1	300	60/60	1020	40 135	20
			940	40 135	
<i>Rb. sphaeroides</i> R-26 pheophytin-modified	300	30/30	1020	9 33 130 320	22
			935	9 130	
<i>Rb. sphaeroides</i> R-26	300	25/25	1020	9 32 82 102 130 172 242 330 935 9 27 43 66 86 130 164 340 760 9 32 51 84	23
<i>Rb. sphaeroides</i> R-26 pheophytin-modified (in dry film)	90	25/25	1020	9 32 52 67 124 324	24
			935	9 25 50 93 122 147 179 325	
<i>Rb. sphaeroides</i> R-26 pheophytin-modified (in glycerol-H ₂ O buffer)	90	25/25	1020	9 32 94 125 158 187 324	24
			935	9 66 93 125 158 188 222 430	
<i>Rb. sphaeroides</i> R-26 native (in glycerol-H ₂ O buffer)	90	25/25	1020	9 32 66 96 127 159 190 223 340	24
			935	9 93 125 164 194 332	
			760	32 64 92	
<i>Rb. sphaeroides</i> R-26 native (in glycerol-D ₂ O buffer)	90	25/25	1020	9 24 72 96 123 148 187 324	24
			935	9 69 96 121 225	
			760	24 48	

^a The data were obtained by pump–probe, resonance Raman (RR), and hole-burning (HB) studies.

phenomenological width of the vibronic transitions), but no quantitative fitting of the experimental data was attempted.

Notice that the Redfield theory implies a density matrix picture in the vibrational eigenstate basis with one or two modes taken into account explicitly, i.e., included as system coordinates. For a larger number of collective nuclear coordinates, a dispersed polaron model (based on the eigenstate-free cumulant expansion method) can be used.⁸ It was shown that, using an arbitrary number of modes, it is possible to define two reaction coordinates coupled to the photoexcitation of primary donor and to electron transfer, respectively. The time evolution of the electron-transfer coordinate (including oscillations and vibrational relaxation) can be calculated for the P* state, but the dynamics of P⁺B⁻ state (including transfer of coherences from the P*) cannot be obtained so easily, because the theory of energy/electron transfer in the dispersed polaron model³⁰ is currently developed only for equilibrated vibrational modes. Thus, Ando and Sumi⁸ used the semiclassical approximation for electron-transfer dynamics. In this approach, the coherent dynamics of the P* state determines an oscillating rate constant for the P* → P⁺B⁻ electron transfer, but no information about dynamics in the photoproduct P⁺B⁻ state is available.

The oscillatory dynamics of the two reaction coordinates can be obtained by applying the Langevin equation.⁹ It was demonstrated that two low-frequency modes (20 and 150 cm⁻¹) are needed to obtain the P⁺B⁻ population dynamics having the same features as the measured TA kinetics at 1020 nm. However, a direct calculation of the kinetics of the spectral response is not possible because the Langevin equation does not contain the coherences between the electronic states (that determine the initial conditions and the relation between the excited-state populations and spectral responses). For quantitative and self-consistent modeling, the full density matrix (in

the basis of the ground, single-, and double-excited electron-vibrational states) is needed.

In this paper, we use a density matrix picture in the vibrational eigenstates basis in order to model the electron-vibrational dynamics in the RC together with its spectral signatures. Our goal is to visualize the time-dependent electron-vibrational wave packet on a potential-energy surface depending on the two reaction coordinates. The diabatic states include an excited state of the primary donor (i.e., special pair, P), and a charge transfer state (P⁺B⁻, which is the primary photoproduct in the pheophytin-modified RC). The mixing of these states (with different displacements along each of the two coordinates) results in a complicated potential-energy surface that determines the time-dependent dynamics of the initially created wave packet (including oscillatory motions, quasireversible charge transfer, and relaxation to the equilibrium position of the primary product). The relaxation dynamics was obtained by including the Redfield relaxation operator in the density matrix equation. The parameters of the electronic states, nuclear modes, and their couplings to the thermal bath (inducing electron-vibrational relaxation) were adjusted from a fit of this model to the experimental pump–probe kinetics in the P* and P⁺B⁻ regions of the pheophytin-modified *Rb. sphaeroides* R-26 RC.²²

The Model

In the pheophytin-modified *Rb. sphaeroides* R-26 RC, an electronic excitation of the special pair P is followed by electron transfer from P to monomeric BChl B_A. The P⁺B⁻ state is a relatively long-lived primary photoproduct (due to the blocked electron transfer to pheophytin). This state is characterized by the absorption band (P⁺B⁻ → P⁺(B⁻)^{*} transition) peaking at 1020 nm, i.e., far from the ground-state absorption of P (870 nm), ESA of P* (upper exciton level near 810 nm), and SE of

the P^* (900–950 nm). Measuring the TA in the 900–950- and 1020-nm regions has allowed us to study separately the decay of the P^* and formation of the P^+B^- state.

The modeling of TA in the 900–1020-nm region should be done in a basis of the ground state, one-exciton manifold containing two diabatic states P^*B and P^+B^- , and two-exciton manifold given by one double-excited state $P^+(B^-)^*$. These four electronic states (labeled by g , e_1 , e_2 , and f , respectively) are coupled to two collective vibrational modes (depending on nuclear coordinates x and y) with the frequencies Ω_x and Ω_y . Dimensionless displacements of the electronic surfaces along the x and y coordinates are given by $\Delta^x = \{\Delta_g^x, \Delta_{e_1}^x, \Delta_{e_2}^x, \Delta_f^x\}$ and $\Delta^y = \{\Delta_g^y, \Delta_{e_1}^y, \Delta_{e_2}^y, \Delta_f^y\}$. The difference between the transition energies of the e_1 and e_2 states is $\epsilon_{12} = \epsilon_1 - \epsilon_2$ (here we calculate the transition energy as the difference in energy between the minima of the potential-energy surfaces involved). The interaction energy between these two states is M_{12} . The Δ^x , Δ^y , Ω_x , Ω_y , ϵ_{12} , and M_{12} values determine the structure of the excited-state eigenfunctions that can be obtained by diagonalization of the exciton-vibrational Hamiltonian (see Appendix). The absolute values of the $P \rightarrow P^*$ and $P^+B^- \rightarrow P^+(B^-)^*$ transition energies were adjusted in order to reproduce the positions of the 870- and 1020-nm absorption maxima. We suppose that only the P^* diabatic state is dipole allowed. The charge-separated P^+B^- state is forbidden, i.e., does not contribute to the ground-state absorption, but exhibits some excited-state absorption to the $P^+(B^-)^*$ state. The corresponding transition dipole value (which is significantly smaller than that of the P^* state) was adjusted in order to reproduce the amplitude of the 1020-nm absorption changes.

The exciton-vibrational dynamics was described by the density matrix equation with the full Redfield tensor, i.e., including all nonsecular terms (see Appendix). The system-bath coupling strength is characterized by $\eta = \{F^2\tau_c, f_x^2\tau_c, f_y^2\tau_c\}$, where F is fluctuation amplitude for electronic coordinates (the same for all electronic states), f_x and f_y are fluctuation amplitudes for x and y vibrational coordinates (not depending on the electronic state), τ_c is the bath relaxation time. A coupling of the electronic states to the bath is included to account for pure exciton relaxation. Such a relaxation becomes dominant in the case of small nuclear reorganization between two excited states. We neglect the off-diagonal coupling, i.e., bath-induced modulation of interaction energy M_{12} . We also suppose that fluctuations acting on different sites and different system coordinates (electronic and two vibrational) are uncorrelated.

Results

The measured and calculated TA kinetics at 900 and 935 nm in the SE region and 1020 nm in the ESA region are shown in Figure 1. The RCs were excited at 870 nm by a 30-fs pulse at room temperature. Parameters of the fit shown in Figure 1 are $\Omega_x = 130 \text{ cm}^{-1}$, $\Omega_y = 32 \text{ cm}^{-1}$, $\Delta^x = \{-0.5, -2.0, 1.3, 2.5\}$, $\Delta^y = \{-1.5, -1.5, 0.5, -1.6\}$, $\eta = \{45, 90, 110\} \text{ cm}^{-1}$, $\epsilon_{12} = 230 \text{ cm}^{-1}$, $M_{12} = 40 \text{ cm}^{-1}$. Frequencies Ω and couplings η can be easily determined from the oscillatory pattern (i.e., periods and decay rates of the high- and low-frequency oscillations). Displacements along nuclear coordinates Δ and energy shift between diabatic states e_1 and e_2 together with the coupling between them M_{12} determine the shape of the excited-state potential surface. The interaction between the P^*B and P^+B^- states results in two excited-state potential surfaces. The lowest one is shown in Figure 2 (although the upper state is not shown in Figure 2, both the lower and higher excited states have been included explicitly in numerical calculations). The initially

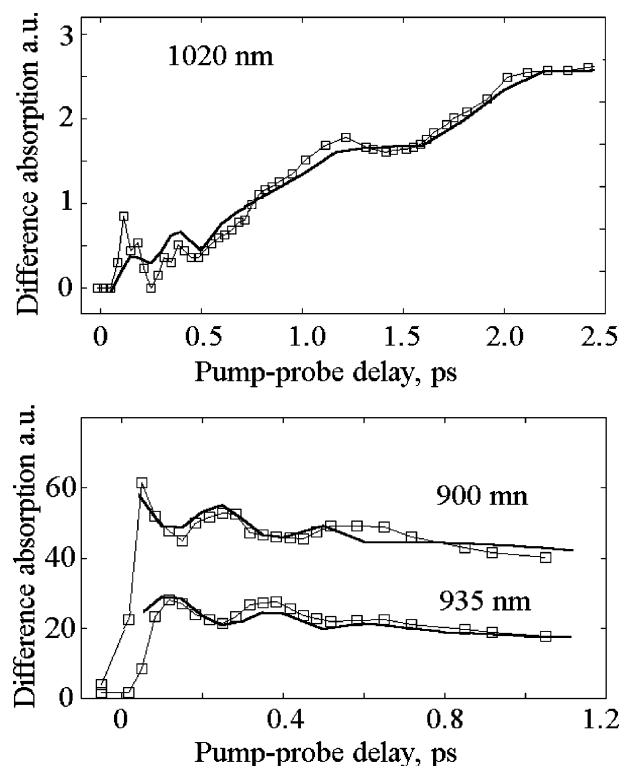


Figure 1. The measured ($-\square-$) and calculated ($-$) TA kinetics at 900, 935, and 1020 nm. Excitation at 870 nm by 30-fs pulse at room temperature. Parameters of the model: $\Omega_x = 130 \text{ cm}^{-1}$; $\Omega_y = 32 \text{ cm}^{-1}$; $\Delta^x = \{-0.5, -2.0, 1.3, 2.5\}$; $\Delta^y = \{-1.5, -1.5, 0.2, -1.4\}$; $\eta = \{45, 90, 110\} \text{ cm}^{-1}$; $\epsilon_{12} = 230 \text{ cm}^{-1}$; $M_{12} = 40 \text{ cm}^{-1}$. The experimental data was taken from ref 22, where the 1020-nm signal was determined as the actual TA value minus the SE background at this wavelength. Correspondingly, the calculated 1020-nm curve is given by the pure ESA without SE background. The TA kinetics at 900 and 935 nm are inverted (the actual TA values are negative been determined by the negative SE contribution).

created wave packet oscillates in the P^* well (along the x coordinate) and penetrates little by little into the P^+B^- well through the barrier between the two surfaces. Figure 2 shows the wave packet near the crossing point between the P^* and P^+B^- potentials (at 248-fs delay). Some part of this wave packet flows into the product region going over the barrier along the x coordinate and shifting in the y direction. The configuration of the mixed e_1 and e_2 states determines the dynamics of the $P^* \rightarrow P^+B^-$ transfer, including the oscillatory features. The configuration given above (i.e., Δ^x , Δ^y , ϵ_{12} , and M_{12} values) corresponds to the best fit of the data. Below we will also discuss alternative schemes.

We start with the time evolution of the wave packet immediately after excitation. Figures 3 and 4 show the wave-packet dynamics during two periods of the 130-cm^{-1} oscillations, i.e., from 0- to 496-fs delays with the step of 62 fs corresponding to a quarter period. First of all, notice that the ground state is shifted with respect to P^* only along the x coordinate. It means that the initial wave packet will be shifted (and will oscillate) only along the x coordinate. (This is not completely true due to mixing of the P^* and P^+B^- states, inducing some time-dependent modulation of the P^* wave packet in the y direction as shown in Figure 3, the 0- and 496-fs frames. Notice in this respect that the experiment showed a presence of higher harmonics of the 32-cm^{-1} mode in the SE kinetics at 900–950 nm,²⁴ providing experimental evidence for such mixing.) The displacement of the ground state along the x coordinate (fast 130-cm^{-1} mode) is between those of the e_1 and

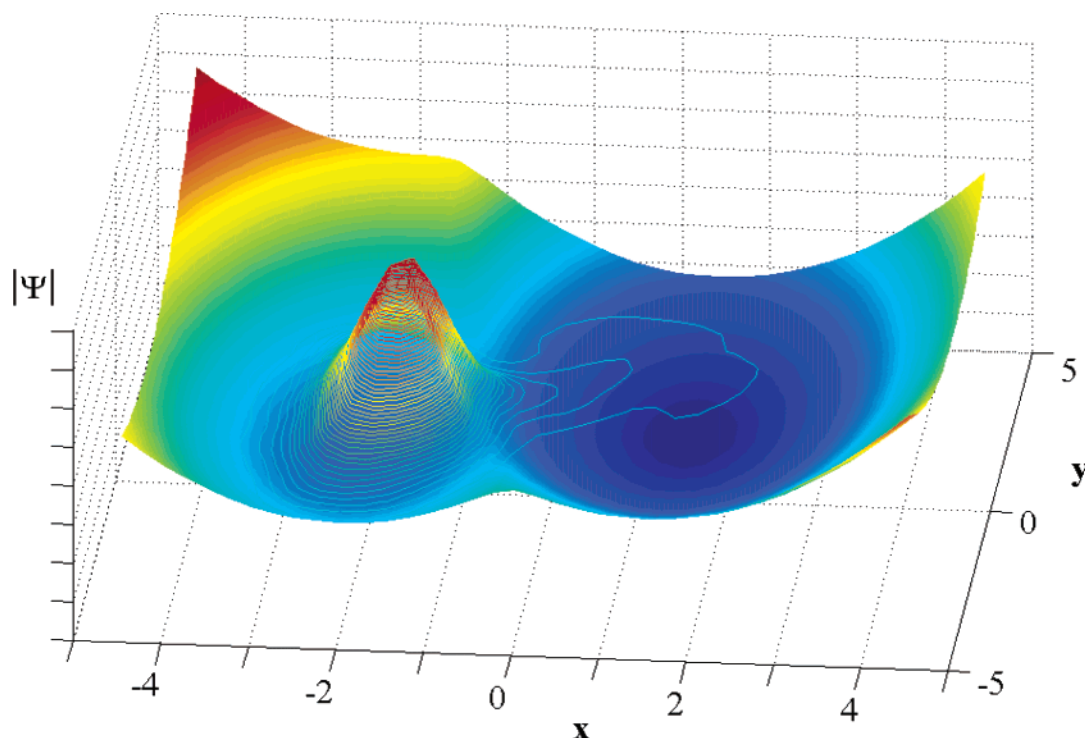


Figure 2. The lowest excited-state potential surface determined by a mixing of the P^*B and P^+B^- states. The x and y coordinates correspond to the two nuclear modes. 3D contour shows the nuclear wave packet (absolute value of $\Psi(x,y,\tau)$ defined in Appendix) at fixed pump–probe delay ($\tau = 248$ fs). Parameters are the same as in Figure 1.

e_2 states so that the initially created wave packet is located at the “right side” of the P^* potential (see Figure 2) near the crossing point between the e_1 and e_2 potential surfaces (with the maximum of the excitation density at $x = -1.3$). Immediately after excitation, the wave packet starts to move to the “left edge” of the P^* potential, i.e., to the long-wavelength region. Some small part of the wave packet starts to move in the opposite direction “to the right”, i.e., into the photoproduct region (see the 62-fs panels in Figures 3 and 4). After a half period of the 130-cm^{-1} mode (124-fs panels in Figures 3 and 4), the main part of the wave packet reaches the long-wavelength side of the P^* state, whereas the minor charge-transfer part reaches the opposite side of the P^+B^- state. At this moment, the SE at 935 nm and the ESA at 1020 nm show an oscillatory maximum. During the next half period, both parts move toward each other and, finally, meet near the potential crossing point (see the 248-fs panels in Figures 3 and 4). Here some part of the P^* wave packet passes over the crossing point, thus increasing the excitation density in the P^+B^- region. It looks like synchronous pumping of the oscillating P^+B^- wave packet. In the model, the fraction of the excitation density passing the crossing point is determined by the relaxation tensor connecting the vibronic states of the two potential wells. The latter depends on the coupling strength η and on the vibronic wave function overlap near the crossing point (which is proportional to the coupling M_{12} between the diabatic states). During the second period (248–496 fs), the wave packet dynamics is basically the same. Notice that during these delays there is some interplay between the x and y coordinates in the photoproduct region with pronounced two-dimensional dynamics (compare the 372-, 434-, and 496-fs panels). This is in contrast to the P^* region, where the wave packet moves only in the x direction, because the ground state is not shifted in the y coordinate and the initial wave packet is centered at $y = -1.5$, corresponding to the minimum of the P^* surface along the y coordinate.

The three bottom frames of Figure 3 show the dynamics at large delays of 992, 1488, and 1984 fs (the difference between these values is about half the 32-cm^{-1} oscillatory period). For large delays, the 130-cm^{-1} mode is almost equilibrated, whereas the 32-cm^{-1} mode is more long-lived, giving rise to oscillations of the wave packet along the y coordinate in the P^+B^- state (mirrored by oscillations of the 1020-nm kinetics as shown in Figure 1).

The 3D representation of the wave packet in Figures 3 and 4 allows a visualization of the main features of the charge-separation dynamics. More details can be obtained from a 2D plot of the wave packet at fixed x or y (Figures 5 and 6). Figure 5 shows the high-frequency (130-cm^{-1}) oscillations in the P^* and P^+B^- regions. At $y = -1.0$ (i.e., close to minimum of the P^* surface), the P^* wave packet exhibits damped oscillations along the x axis. It is interesting that the amplitude of these oscillations decreases upon tuning out of the P^* minimum (for example, in the $y > 0$ region), implying that only the central part of the P^* wave packet is oscillating. These oscillations induce transfer to the product region when the P^* wave packet approaches the barrier between the P^* and P^+B^- potentials. Transfer of some part of the excitation density to the P^+B^- region is accompanied by a shifting of this part of the wave packet to the region near $y = 0$ within the P^+B^- potential (because the barrier between P^* and P^+B^- states at $y = 0$ is lower than at $y = -1.5$) and further shifting to the $y = 2$ region due slow oscillatory dynamics of the low-frequency mode. (Notice that the minimum of the P^+B^- potential corresponds to $y = 0.5$). The P^+B^- wave packet oscillates with the opposite phase with respect to the P^* wave packet (the P^* and P^+B^- parts are always going in the opposite directions along the x axis).

The 0–496-fs time period corresponds to two periods of the 130-cm^{-1} oscillations along the x axis and to one-half of a period of the 32-cm^{-1} oscillations along the y axis. Thus, the oscillatory

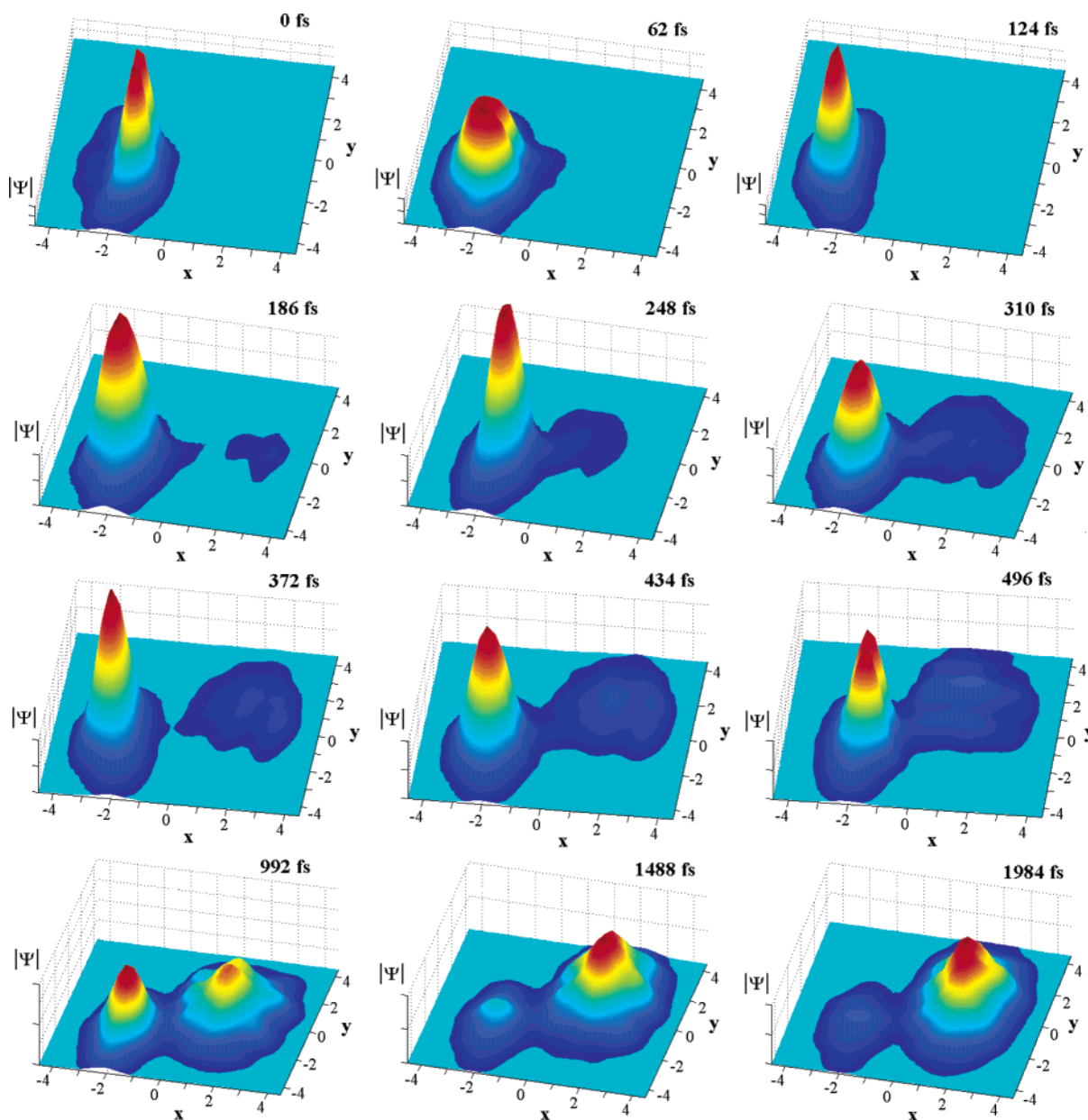


Figure 3. Dynamics of the wave packet in the plane of nuclear coordinates x and y (the same coordinates as shown in Figure 2). Delays from 0 to 496 fs are shown with the step of 62 fs (approximately one quarter of the 130-cm^{-1} oscillatory period). The three bottom panels correspond to delays 992, 1488, and 1984 fs (i.e., separated by one half of the 32-cm^{-1} oscillatory period). The z -axis scale (corresponding to absolute values of $\Psi(x,y,\tau)$ in arbitrary units) is the same for all panels. Parameters are the same as in Figure 1.

features in the x direction during 0–496 fs coincide with the shift of the P^+B^- wave packet maximum from $y = 0$ to $y = 2$. During the second half period of the low-frequency oscillations (496–992 fs), the maximum shifts back to $y = 0$ (Figure 6). For larger delays, there is a damped oscillatory behavior along the y axis in the P^+B^- region. The x oscillations are not so pronounced at large delays.

Other Configurations (Opposite Displacement of the Ground State). The results shown in Figures 1–6 correspond to $\Delta^x = \{-0.5, -2.0, 1.3, 2.5\}$ when the ground-state minimum ($\Delta_g^x = -0.5$) is between those of the e_1 and e_2 states, i.e., $\Delta_{e_1}^x = -2.0$ and $\Delta_{e_2}^x = 1.3$. For this configuration, the initially created wave packet is located near the surface-crossing point at $x = -1.3$. After excitation, its main part starts to move to the $x < -2.0$ region in the P^* potential, whereas a minor part penetrates the P^+B^- region moving in the opposite direction toward the $x > 1.5$ region. After the half period ($\tau = \pi/\Omega_x$), the Franck–Condon regions for the $\text{P}^* \rightarrow \text{P}$ stimulated emission

and $\text{P}^+\text{B}^- \rightarrow \text{P}^+(\text{B}^-)^*$ absorption are reached, giving rise to maxima in the absolute values of SE and ESA (as shown in Figure 1).

In an alternative configuration $\Delta^x = \{-3.5, -2.0, 1.3, 0.1\}$, the ground-state minimum ($\Delta_g^x = -3.5$) is at the opposite side of the P^* potential. The $\text{P}^+(\text{B}^-)^*$ minimum ($\Delta^x = 0.1$) also has an opposite shift with respect to that of P^+B^- . For such a configuration, the Franck–Condon regions for both the $\text{P}^* \rightarrow \text{P}$ emission and $\text{P}^+\text{B}^- \rightarrow \text{P}^+(\text{B}^-)^*$ absorption are near the surface-crossing region. The initial wave packet is now moving from the $x < -2.0$ region toward the surface-crossing point. Reaching this point after a half period results in maxima in the –SE and ESA kinetics. Unfortunately, the amplitude of the 1020-nm oscillations is lower in this case, because the excitation penetrates to the P^+B^- region from the P^* wave packet, which has broadened due to dephasing at $\tau = \pi/\Omega_x$. (Remember that in the configuration shown in Figures 1–6 the first potential crossing occurs at $\tau = 0$.) Moreover, the Franck–Condon

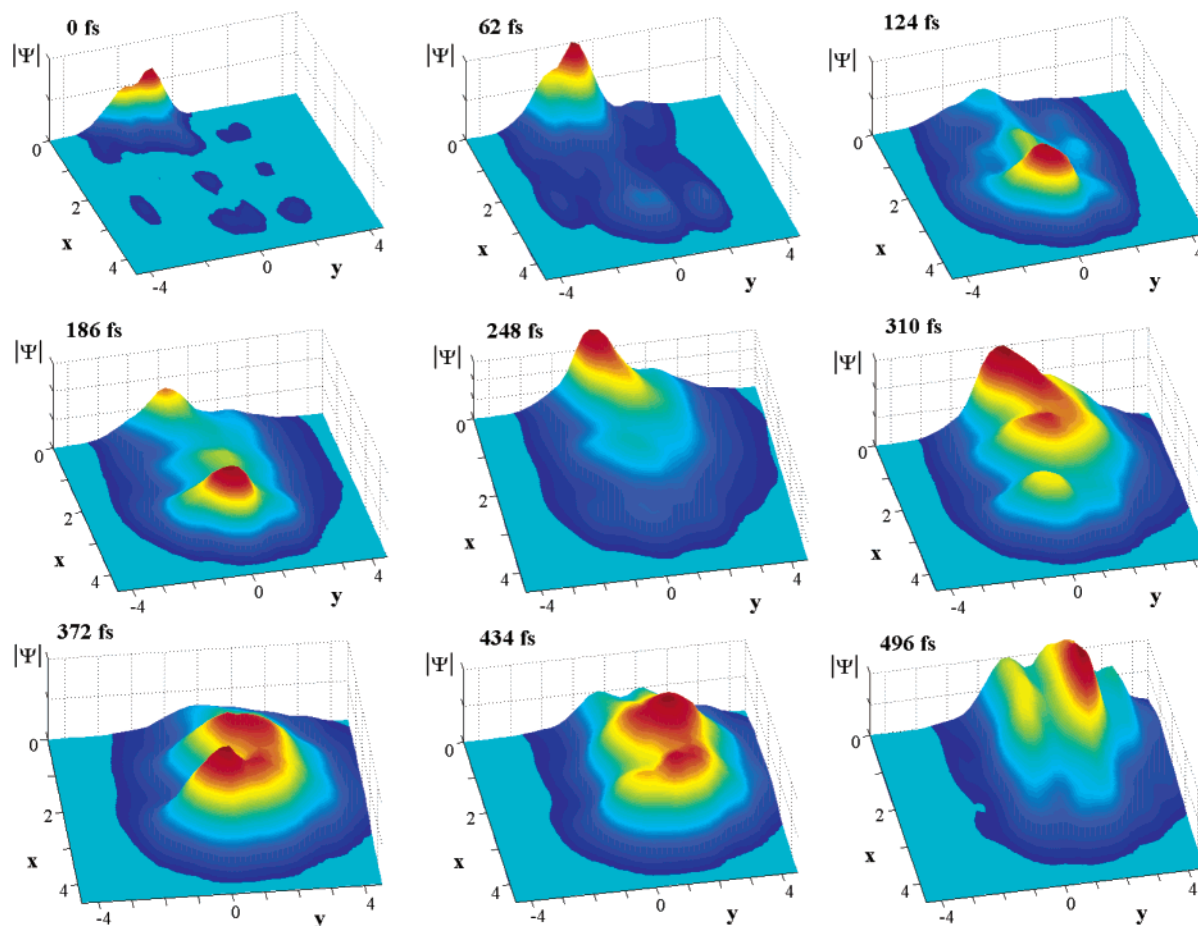


Figure 4. The same as 0–496-fs panels of Figure 3 where only the photoproduct region ($x > 0$) is shown. The z -axis scale is 10% (0, 62, 124 fs), 15% (186, 248, 310 fs), and 20% (372, 434, 496 fs) of the z scale shown in Figure 3.

regions for the $P^+B^- \rightarrow P^+(B^-)^*$ absorption is in fact slightly shifted from the crossing point to positive x values. This gives rise to some phase shift of the 1020-nm oscillations with respect to the measured ones. In principle, this effect could be compensated by a shifting of the $P^+(B^-)^*$ minimum to $\Delta_{\text{f}}^x = -0.5$. But in this case the 1020-nm absorption band becomes too broad as compared with the measured one.²² Then we conclude that this alternative configuration is not so good for a quantitative fit, although it gives a reasonable explanation of the data at a qualitative level.

The relative displacements of the potential-energy surfaces (for both configurations) have been determined from the fit of the TA traces. The oscillatory pattern in the primary donor region (900–935 nm) is determined by the displacement of the P^* state with respect to the ground-state P . Thus, the amplitude of the 130-cm^{-1} oscillations is proportional to the shift of P^* along the x coordinate (in our case, $\Delta_{\text{g}}^x = -0.5$ and $\Delta_{\text{e}_1}^x = -2.0$, so that the P – P^* shift equals to 1.5). The relative amplitudes and phases of the high-frequency (130-cm^{-1}) oscillations in the P^* and P^+B^- regions are strongly dependent on the relative displacements of the corresponding potential energy surfaces along the x coordinate (i.e., on $\Delta_{\text{e}_1}^x$ and $\Delta_{\text{e}_2}^x$). We found that a large value of the P^* – P^+B^- displacement, i.e., $\Delta_{\text{e}_2}^x - \Delta_{\text{e}_1}^x = 3.3$ ($\Delta_{\text{e}_1}^x = -2.0$ and $\Delta_{\text{e}_2}^x = 1.3$) is required to explain the data both for the normal and alternative positions of the ground state (with $\Delta_{\text{g}}^x = -0.5$ and -3.5 , respectively). It is interesting that these two configurations are characterized by different values of the P – P^+B^- shift, i.e., $\Delta_{\text{e}_2}^x - \Delta_{\text{g}}^x = 1.8$ and 4.8, respectively. Although the former gave a better quantitative fit, both of them are in reasonable qualitative

agreement with the experiment. In our model, the P^+B^- state can be reached only through the P^* state and not directly from the ground state. That is why the model is critical with respect to the P^* – P^+B^- shift but not to that of P – P^+B^- . At first sight, it seems that the P – P^+B^- shift must be larger than that of P – P^* , because the more polar charge-transfer state P^+B^- should more strongly reorganize the environment. In this respect, the second (alternative) configuration is more reasonable. However, we still give preference to the first configuration which allows a better fit. Close values of the P^* – P^+B^- and P – P^+B^- shifts for this model possibly reflect the charge-transfer character of the P^* state itself (for example, due to mixing with the $P_2^+P_1^-$ state in which electron transfer has occurred between the two BChls, P_2 and P_1 , of the special pair).

Configurations with Different Displacements along Two Nuclear Modes. We have compared configurations with different displacements of the P^+B^- diabatic state with respect to P^* . In the first example, the P^+B^- state is unshifted along the y direction ($\Delta_{\text{e}_1}^y = \Delta_{\text{e}_2}^y$), but the shift along the x coordinate is the same as in our original configuration. In the second example, the photoproduct state is unshifted along the x and y directions ($\Delta_{\text{e}_1}^y = \Delta_{\text{e}_2}^y$ and $\Delta_{\text{e}_1}^x = \Delta_{\text{e}_2}^x$).

For the first configuration, we found almost the same dynamics (and the same TA kinetics at 900, 935, and 1020 nm) as in the original configuration during the first few oscillatory periods of the 130-cm^{-1} mode, i.e., for delays 0–0.5 ps. For larger delays, the TA kinetics at 900 and 935 nm exhibit a nonoscillatory decay that is slower than in the original configuration. The TA kinetics at 1020 nm at large delay has no low-frequency (32-cm^{-1}) oscillations due to the absence of the

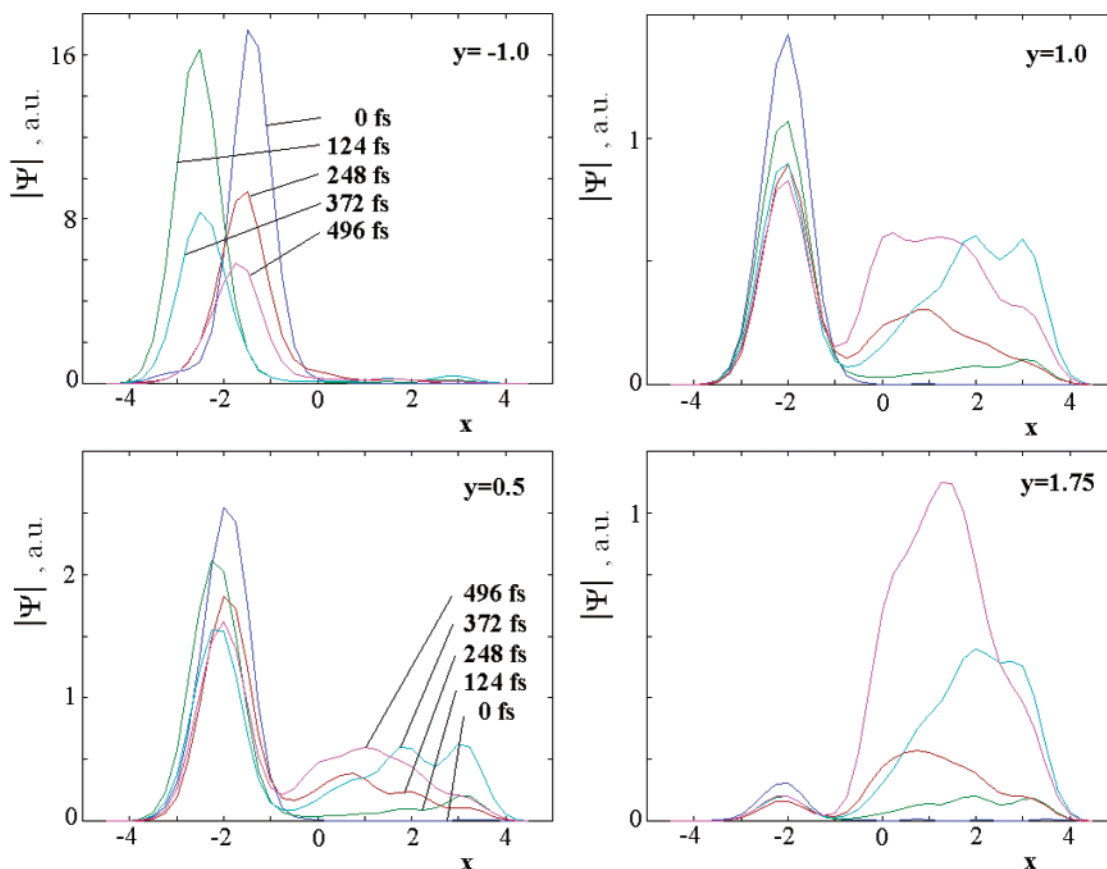


Figure 5. The shape of the wave packet as a function of x at fixed y . Oscillatory dynamics in the P^* region for as 0–496-fs delays is shown together with coherent formation of the P^+B^- state. Parameters are the same as in Figures 1 and 3.

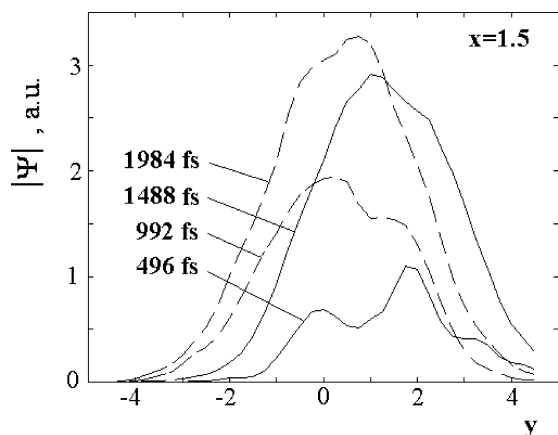


Figure 6. The shape of the wave packet as a function of y at fixed x , corresponding to the P^+B^- region. Low-frequency oscillations along the y coordinate for large delays are shown. Parameters are the same as in Figures 1 and 3.

dynamics along the y coordinate. Again, the nonoscillatory rise of the 1020-nm kinetics is slower (by 20–30% for our parameter set). We conclude that shifting of the wave packet along the y coordinate after its passage from the P^* to P^+B^- state results in a stabilization of the P^+B^- state.

In the second (unshifted) configuration, the $P^* \rightarrow P^+B^-$ transfer is given by purely electronic relaxation (because the nuclear coordinates are the same for the two electronic states). The relaxation rate depends on the fluctuation amplitudes for the electronic coordinate, F_{e1} and F_{e2} , respectively, and also on the mixing of the electronic wave functions of the P^* and P^+B^- states (this mixing is given by the ratio M_{12}/ϵ_{12} between the interaction energy and the energy gap between the diabatic

states). In this case, for our parameter set, the calculated rate of the $P^* \rightarrow P^+B^-$ transfer is slower than that for the shifted configurations.

Energetic Disorder of the Special Pair and Photoproduct States. In the modeling shown in Figures 1–6, we use fixed values of the $P^* \rightarrow P$ and $P^+B^- \rightarrow P^+(B^-)^*$ transition energies (corresponding to 870 and 1020 nm), the $P^*-P^+B^-$ energy difference of $\epsilon_{12} = 230 \text{ cm}^{-1}$, and $P^*-P^+B^-$ coupling of $M_{12} = 40 \text{ cm}^{-1}$. In reality, these values will be perturbed due to static disorder (random shift of the energies ϵ_1 and ϵ_2 of the diabatic states and shift of the interaction energy M_{12}). There are serious numerical problems in including the static disorder into our modeling. We found that the manifold of excited states should include about 100 vibronic sublevels to obtain a realistic picture of electron-vibrational dynamics (a further increase of the number of states does not change significantly the oscillatory pattern but leads to an exponential increase of the computing time). The corresponding density matrix is then given by a set of 10 000 equations with the Redfield tensor consisting of $10\,000 \times 10\,000$ elements. A considerable computing time (typically a couple of hours with a 2.5-GHz processor) is needed to calculate the nonlinear response just for one realization of the disorder with fixed parameters Ω_x , Ω_y , $\Delta^x = \{\Delta_g^x, \Delta_{e1}^x, \Delta_{e2}^x, \Delta_f^x\}$, $\Delta^y = \{\Delta_g^y, \Delta_{e1}^y, \Delta_{e2}^y, \Delta_f^y\}$, and $\eta = \{F^2\tau_c, f_x^2\tau_c, f_y^2\tau_c\}$. A fitting procedure (implying variation of these parameters) becomes a difficult task even without averaging over the various realizations of the disorder.

Although we are not able to make an averaging over disorder, we have studied how shifting the energies (for ϵ_1 , ϵ_2 , and ϵ_{12}) influences the excited-state dynamics. We found that a variation of the $P^*-P^+B^-$ energy difference in the $\epsilon_{12} = 130\text{--}330\text{-cm}^{-1}$ range (at fixed $P^* \rightarrow P$ energy, ϵ_1) does not change significantly

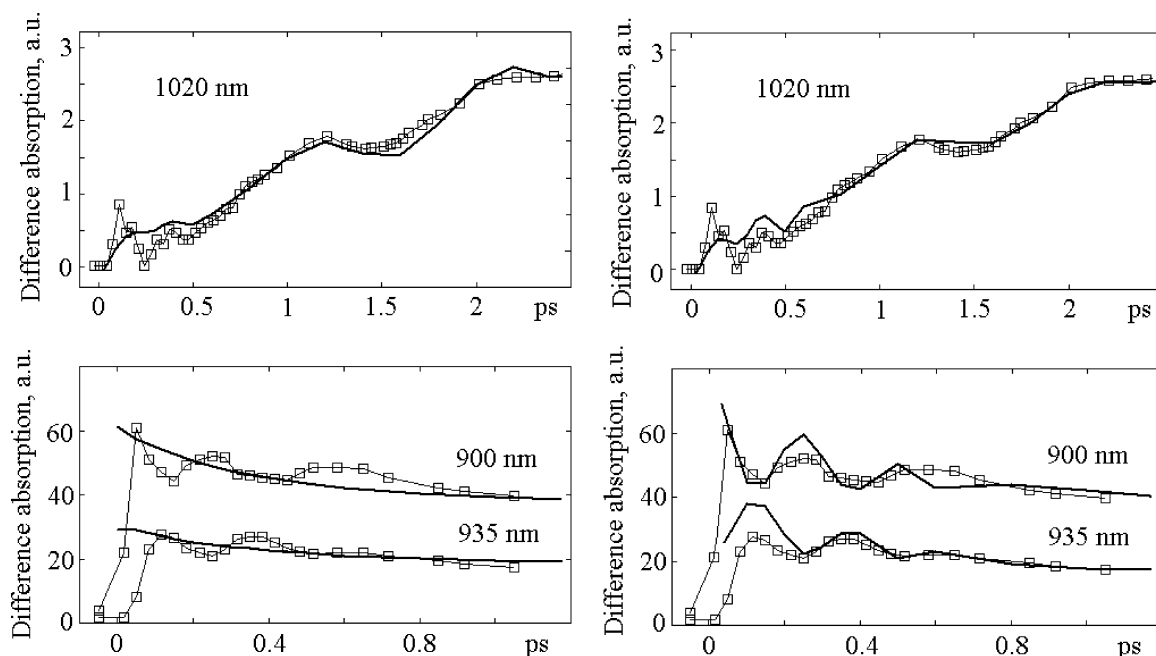


Figure 7. The same as in Figure 1 with the energy of the $P^* \rightarrow P$ transition (ϵ_1) shifted by 150 cm^{-1} (two left frames) or -150 cm^{-1} (two right frames). The energy difference between the P^* and P^+B^- states ϵ_{12} was kept the same as in Figure 1.

the dynamics of $P^* \rightarrow P^+B^-$ transfer, i.e., does not destroy the fit of the 1020-nm kinetics. Also variation of M_{12} from 30 to 50 cm^{-1} has only a minor effect on the calculated kinetics. Variation of the $P^* \rightarrow P$ energy by $\pm 150 \text{ cm}^{-1}$ (with fixed ϵ_{12} value) has a minor effect on the 1020-nm kinetics but changes significantly the amplitude of the 900–950-nm oscillations. Thus, a decrease in ϵ_1 by 150 cm^{-1} (with a fixed wavelength of the pump pulse) results in the excitation of higher vibronic levels of P^* , giving rise to a larger amplitude of the wave-packet oscillations within the P^* potential surface and stronger oscillations of TA in the 900–950-nm region (Figure 7, two right frames). In the case of higher ϵ_1 values, the pump pulse interacts only with the lowest levels of the 130-cm^{-1} mode. As a result, the TA oscillations in the 900–950-nm region are significantly reduced. If we increase ϵ_1 by 150 cm^{-1} , the oscillatory features in the 900–950-nm region disappear completely (Figure 7, two left frames). Interestingly, in this case, the 1020-nm oscillations still exist, with a smaller amplitude of the 130-cm^{-1} oscillations and almost the same amplitude of the low-frequency 30-cm^{-1} oscillations. Notice that the vibrational coherence transfer from the P^* to P^+B^- states is determined by nonsecular terms of the Redfield tensor. In this case, vibrational coherence can be created in a photoproduct even if the initial state has a little or no vibrational coherence. This effect was originally pointed out by Jean and Fleming.⁷

From Figures 1 and 7, we can infer that an averaging over the ϵ_1 disorder (with the $200\text{--}300\text{-cm}^{-1}$ width) most probably will not change significantly the oscillatory amplitudes. On the other hand, if the disorder value exceeds $200\text{--}300 \text{ cm}^{-1}$, an explicit averaging over all possible realizations is needed. Approximately the same estimation can be done for a possible disorder of the photoproduct state.

The Spectral Density Choice. In our modeling, we used the frequency-independent spectral density (see Appendix). We also used other spectral densities, in particular the ohmic spectral density ($\sim \omega \exp(-\omega/\omega_c)$ with the maximum near ω_c). Varying the ω_c value from 100 to 800 cm^{-1} , we were able to obtain

almost the same picture as shown in Figure 1 (for each ω_c value, we did some adjustment of the coupling strengths for both modes).

Discussion and Conclusion

Comparison with Molecular Dynamics Simulations. Path-integral simulation of charge-transfer dynamics in the native and pheophytin-modified *Rhodobacter sphaeroides* RCs³¹ suggested values for $\epsilon_{12} = 400 \text{ cm}^{-1}$ and for $M_{12} = 22 \text{ cm}^{-1}$. The coupling to nuclear degrees of freedom was modeled by assuming an ohmic spectral density ($\sim \omega \exp(-\omega/\omega_c)$ with the maximum near $\omega_c = 600 \text{ cm}^{-1}$) as well as by a spectral density calculated from a molecular dynamic calculation. In the latter case, there is more pronounced coupling to low-frequency modes (with the maximal density in the $100\text{--}200\text{-cm}^{-1}$ region). Notice that in our modeling the low-frequency modes (below 200 cm^{-1}) are taken into account explicitly as system coordinates, thus allowing the simulation of vibrational coherence dynamics (not included in the model of Sim and Makri).³¹ To model the coupling of these two modes with the remaining nuclear degrees of freedom (i.e., not included as a system coordinates), we used the frequency-independent as well as the ohmic spectral density. To reproduce the oscillatory features and the time scale of photoproduct formation, we need $\epsilon_{12} = 130\text{--}330 \text{ cm}^{-1}$ and $M_{12} = 30\text{--}50 \text{ cm}^{-1}$ values, giving a configuration of potential surfaces close to that proposed by Sim and Makri.

Other molecular dynamics simulations suggested $\epsilon_{12} = 400\text{--}700 \text{ cm}^{-1}$ values (see, for review, of Warshel and Parson⁴ and references therein). The electronic coupling energy was estimated as $M_{12} = 25 \text{ cm}^{-1}$ ⁴ and $M_{12} = 35 \text{ cm}^{-1}$.³²

Dynamical Effects in Charge Separation. The coupling of electron transfer in the RC to nuclear modes as observed experimentally has led to the question of the role of dynamical effects in charge separation. The question is whether the motion along a particular vibrational coordinate can increase the rate of charge transfer from the reactant to the primary photoproduct. From molecular dynamics simulations, it was concluded that the charge-transfer kinetics is given by the probability of

reaching the surface-crossing point through random thermal motions and not by special dynamical effects.⁴ Our results show that the possibility to reach the surface-crossing point is not connected with the random thermal motion of many nuclear modes but is given by the dynamics of a specific mode, i.e., the high-frequency (130-cm⁻¹) mode, which determines the first reaction coordinate in our scheme. In our model, the structure of the potential surfaces is determined by the combined action of the two modes with specific displacements. Thus, the potential barrier (and the energy difference) between the P* and P⁺B⁻ states is not large along the first coordinate (given by the 130-cm⁻¹ mode). This results in a good overlap between the 130-cm⁻¹ vibronic sublevels belonging to the P* and P⁺B⁻ wells. As a result, the rate of P* → P⁺B⁻ penetration is high both in coherent and incoherent cases. After the first passages through the crossing point, the wave packet shifts to the minimum of the P⁺B⁻ state, which is given by a displacement of the 32-cm⁻¹ mode along the second reaction coordinate. This leads to the irreversible character of charge transfer. Thus, a combination of the two specific modes creates a configuration of the states with a high transfer rate together with a low probability for back transfer. One of these modes (130 cm⁻¹, probably connected with the intermolecular dynamics within the special pair) determines an efficient tunneling through the barrier, whereas the other (32 cm⁻¹, connected with the polar environment of the product) is responsible for a stabilization of the primary charge-separated state. The presence of vibrational coherence in the experiment allows a visualization of this dynamics and determination of the corresponding potential surface configuration. But the efficiency of the transfer dynamics is not connected with a coherent character of nuclear modes. Thus, in the absence of vibrational coherences in the P* band, the charge-separation dynamics is almost the same as in the coherent case (Figure 7). An important conclusion is that the charge-separation dynamics (both for coherent or noncoherent excitation) is determined by coupling to two specific nonequilibrated vibrational coordinates leading to efficient photoproduct formation.

Conclusions

We have modeled the primary charge-separation dynamics coupled to a coherent nuclear motion in the pheophytin-modified *Rhodobacter sphaeroides* R-26 RC. The model includes two diabatic states, i.e., an excited-state P* of the primary donor (i.e., special pair, P) and a charge-transfer state (P⁺B⁻, which is the primary photoproduct in the pheophytin-modified RC). The strong coupling of these states with two collective nuclear modes is supposed. The mixing of diabatic states (with different displacements along each of the two nuclear coordinates) results in a complicated potential surface that determines the efficient and quasi-irreversible electron transfer through the barrier between the P* and P⁺B⁻ states. The model allowed us to obtain a quantitative fit of the experimental kinetics of the P* → P SE near 900–950 nm and the P⁺B⁻ → P⁺(B⁻)^{*} ESA in the 1020-nm region of the pheophytin-modified *Rhodobacter sphaeroides* R-26 RC. By use of the parameters adjusted from the fit, we obtained a direct visualization of the electron-vibrational wavepacket evolution, including the surface-crossing dynamics superimposed with oscillatory motion along two reaction coordinates in the P* and P⁺B⁻ states. Quantitative modeling of the coherent nuclear dynamics allowed a determination of the specific configuration of two vibrational coordinates responsible for an efficient charge separation.

Acknowledgment. The research was supported by the Russian-Dutch Research Cooperation Program (NWO, 047.009.014) and by the Russian Foundation for Basic Research, Grant No. 02-04-48779.

Appendix

Exciton-Vibrational Hamiltonian. The system consists of the ground state, one-exciton manifold containing two diabatic states P*B and P⁺B⁻, and two-exciton manifold given by one double excited-state P⁺(B⁻)^{*}. These electronic states are coupled to two vibrational coordinates. The system (exciton-vibrational) Hamiltonian is

$$H_{\text{ex-vib}} = H_g + H_e + H_f$$

$$H_g = |g\rangle h(\epsilon_g, \Delta_g^x, \Delta_g^y) \langle g|$$

$$H_e = |e_1\rangle h(\epsilon_{e_1}, \Delta_{e_1}^x, \Delta_{e_1}^y) \langle e_1| + |e_2\rangle h(\epsilon_{e_2}, \Delta_{e_2}^x, \Delta_{e_2}^y) \langle e_2| + |e_1\rangle M \langle e_2| + |e_2\rangle M \langle e_1|$$

$$H_f = |f\rangle h(\epsilon_f, \Delta_f^x, \Delta_f^y) \langle f|$$

$$h(\epsilon, \Delta^x, \Delta^y) = \epsilon + \Omega_x \left(\beta_x^+ \beta_x + \frac{1}{2} \right) - \left(\frac{1}{2^{1/2}} \right) \Omega_x \Delta^x (\beta_x + \beta_x^+) + \Omega_y \left(\beta_y^+ \beta_y + \frac{1}{2} \right) - \left(\frac{1}{2^{1/2}} \right) \Omega_y \Delta^y (\beta_y + \beta_y^+)$$

The basic states are given by a direct product of the electronic (g, e₁, e₂, and f) and two vibrational wave functions (a_x and a_y). These vibrational wavefunctions depending on x and y coordinates are supposed to be unshifted (i.e., have zero displacements along x and y). The creation and annihilation phonon operators β⁺ and β are working in this unshifted basis. A displacement of the electronic surfaces along the x and y coordinates Δ^x and Δ^y are described in this basis by shifting operators Ω_xΔ_x(β_x + β_x⁺)/2^{1/2} and Ω_yΔ_y(β_y + β_y⁺)/2^{1/2}, where Ω_x and Ω_y are the frequencies of nuclear modes corresponding to the x and y coordinates. Each diabatic state (g, e₁, e₂, and f) is characterized by the frequencies Ω_x and Ω_y, dimensionless displacements Δ^x and Δ^y, and energy ε. Electronic transitions between diabatic states generally include the g → e₁, g → e₂, e₁ → f, and e₂ → f transitions with the electronic transition dipoles **d**₁, **d**₂, **d**_{f1}, and **d**_{f2} and transition energies ε_{e1} - ε_g, ε_{e2} - ε_g, ε_f - ε_{e1}, ε_f - ε_{e2}. The transition energies counted as the difference between the minimums of the corresponding potential surfaces include a reorganization energy values. For example, for the g → e₁ transition, the difference between the e₁ and g potential minimums is ε_{e1} - ε_g - Ω_xS_x - Ω_yS_y, depending on Huang–Rhys factors S_x = (Δ_{e1}^x - Δ_g^x)²/2 and S_y = (Δ_{e1}^y - Δ_g^y)²/2 that are given by the corresponding relative displacements. The interaction between excited states (e₁, e₂) is given by the energy M that is independent of vibrational coordinates. Diagonalization of the Hamiltonian

$$H_g C^g = C^g E^g; |c\rangle = \sum_a C_{ac}^g |g a_x a_y\rangle; E_{cc}^g = \delta_{cc} \epsilon_c$$

$$H_e C^e = C^e E^e; |b\rangle = \sum_{na} C_{nab}^e |e_n a_x a_y\rangle; E_{bb}^e = \delta_{bb} \epsilon_b$$

$$H_f C^f = C^f E^f; |r\rangle = \sum_a C_{ar}^f |f a_x a_y\rangle; E_{rr}^f = \delta_{rr} \epsilon_r$$

gives the ground, one-exciton, and two-exciton state eigenfunctions (c, b, and r) as a linear combinations of the unshifted basic

functions a_x and a_y . The one-exciton states also include a mixing of the two diabatic states $n = 1, 2$. Indexes a and na number the $|a_x a_y\rangle$ and $|e_n a_x a_y\rangle$ states. Transition dipoles between ground, one-, and two-exciton vibronic manifolds are

$$\begin{aligned}\mu_{cb} &= \sum_{na} C_{ac}^g \mathbf{d}_n C_{nab}^e \\ \mu_{rb} &= \sum_{na} C_{ar}^f \mathbf{d}_{fn} C_{nab}^e\end{aligned}$$

where \mathbf{d}_n and \mathbf{d}_{fn} are ground to one-exciton and one- to two-exciton electronic transition dipoles. In our model, $\mathbf{d}_n \neq 0$ for P^* ($n = 1$), whereas $\mathbf{d}_{fn} \neq 0$ for the charge-transfer state P^+B^- ($n = 2$). Generalization to arbitrary number of one- and two-exciton states is straightforward.

Sequential Pump–Probe. The interaction with the laser field is described by

$$H_E = -\mathbf{E}(t) \left[\sum_{c,b} \mu_{cb} |c\rangle \langle b| + \sum_{r,b} \mu_{br} |b\rangle \langle r| \right] + h.c.$$

$$\mathbf{E}(t) = \mathbf{E}_1(\omega_1, t) + \mathbf{E}_2(\omega_2, t) + c.c.$$

$$\mathbf{E}_1(\omega_1, t) = \mathbf{e}_1 \epsilon_1(t) e^{-i\omega_1 t + ik_1 r}$$

$$\mathbf{E}_2(\omega_2, \tau, t) = \mathbf{e}_2 \epsilon_2(t - \tau) e^{-i\omega_2 t + ik_2 r}$$

The external field is represented by the pump and probe optical pulses with the frequencies ω_1 and ω_2 , wave vectors k_1 and k_2 , polarization vectors \mathbf{e}_1 and \mathbf{e}_2 , and envelopes $\epsilon_1(t)$ and $\epsilon_2(t - \tau)$, respectively (ϵ_1 and ϵ_2 can be complex in the case of frequency modulated pulses). The pump–probe delay is τ .

The pump–probe signal is given by³⁵

$$\Delta A(\omega_1, \omega_2, \tau) = 2\omega_2 \int_{-\infty}^{\infty} dt \operatorname{Im} \{ \mathbf{E}_2^*(\omega_2, \tau, t) \mathbf{P}^{(3)}(\omega_1, \omega_2, \tau, t) \}$$

$$\begin{aligned}\mathbf{P}^{(3)}(\omega_1, \omega_2, \tau, t) = & e^{-i\omega_2 t + ik_2 r} \left\{ \sum_{c,b} \mu_{cb} \rho_{bc}^{(3)}(\omega_2) + \sum_{r,b} \mu_{br} \rho_{rb}^{(3)}(\omega_2) \right\}\end{aligned}$$

where $\mathbf{P}^{(3)}$ denotes the nonlinear (third-order) polarization which is determined by the reduced density matrix $\rho^{(3)}$ in third order with respect to the external field. The polarization should oscillate at frequency ω_2 to contribute to the pump–probe signal. Correspondingly, only the $\rho^{(3)}$ elements oscillating at frequency ω_2 have to be taken into account. The slowly varying amplitudes of these elements can be obtained from the Liouville equation for the reduced density matrix ρ

$$\frac{d\rho}{dt} = -i[H + H_E, \rho] - R\rho$$

where R is the Redfield superoperator describing the relaxation in the limit of weak coupling of the electronic and vibrational coordinates with the thermal bath. The third-order expansion gives (in the rotating wave approximation)

$$\begin{aligned}\left[\frac{d}{dt} + i(\omega_{bc} - \omega_1) \right] \rho_{bc}^{(1)}(\omega_1) &= -[R\rho^{(1)}(\omega_1)]_{bc} + i\epsilon_1 \mu_{bc} P_c \\ \left[\frac{d}{dt} + i\omega_{bb'} \right] \rho_{bb'}^{(2)}(0) &= -[R\rho^{(2)}(0)]_{bb'} + \\ i\epsilon_1 \sum_c \mu_{bc} \rho_{cb'}^{(1)}(-\omega_1) - i\epsilon_1^* \sum_c \rho_{bc}^{(1)}(\omega_1) \mu_{cb'}\end{aligned}$$

$$\begin{aligned}\left[\frac{d}{dt} + i\omega_{cc'} \right] \rho_{cc'}^{(2)}(0) &= -[R\rho^{(2)}(0)]_{cc'} + \\ i\epsilon_1^* \sum_b \mu_{cb} \rho_{bc'}^{(1)}(\omega_1) - i\epsilon_1 \sum_b \rho_{cb}^{(1)}(-\omega_1) \mu_{bc'} \\ \left[\frac{d}{dt} + i(\omega_{bc} - \omega_2) \right] \rho_{bc}^{(3)}(\omega_2) &= -[R\rho^{(3)}(\omega_2)]_{bc} - \\ i\epsilon_2 \sum_{b'} \rho_{bb'}^{(2)}(0) \mu_{b'c} + i\epsilon_2 \sum_{c'} \mu_{bc'} \rho_{c'c}^{(2)}(0) \\ \left[\frac{d}{dt} + i(\omega_{rb} - \omega_2) \right] \rho_{rb}^{(3)}(\omega_2) &= \\ -[R\rho^{(3)}(\omega_2)]_{rb} + i\epsilon_2 \sum_{b'} \mu_{rb'} \rho_{b'b}^{(2)}(0)\end{aligned}$$

where $\omega_{bc} = \epsilon_b - \epsilon_c$, $\mu_{bc} = \mu_{bc} \mathbf{e}_1$, $\mu_{rb} = \mu_{rb} \mathbf{e}_2$ and P_c is the steady-state vibronic population in the ground state. We considered a sequential (time-ordered) pump–probe. In this case, the pump acts first creating an excited-state population and a ground-state hole giving rise to the absorption changes which consist of ESA, SE, and ground-state PB. Sequential limit is valid for delays larger than the pulse duration, whereas for short delays, sequential contribution is superimposed with the coherent artifact due to pump–probe overlap.

Pulses Shorter than Vibrational Relaxation (Snapshot Limit). We suppose that pump and probe pulses are short in the time scale of vibrational relaxation (but not short as compared with the oscillatory dynamics given by $\omega_{bb'}^{-1}$ and $\omega_{cc'}^{-1}$). Then we get

$$\begin{aligned}\text{SE} = -\omega_2 \sum_{cbb'} \mu_{cb} \mu_{b'c} \tilde{\rho}_{bb'}(\tau) e^{-i\omega_{bb'}\tau - (\omega_{bb'}\tau_2)^2/4} \times \\ \int_0^\infty dt e^{-t^2/4\tau_2^2 + i\omega_{bb'}t/2} \{ e^{-i(\omega_{bc} - \omega_2)t - R_{bcb}t} + c.c. \}_{b \rightarrow b'}\end{aligned}$$

$$\begin{aligned}\text{PB} = -\omega_2 \sum_{cc'b} \mu_{cb} \mu_{bc'} \tilde{\rho}_{cc'}(\tau) e^{-i\omega_{cc'}\tau - (\omega_{cc'}\tau_2)^2/4} \times \\ \int_0^\infty dt e^{-t^2/4\tau_2^2 + i\omega_{cc'}t/2} \{ e^{i(\omega_{bc} - \omega_2)t - R_{bcc}t} + c.c. \}_{c \rightarrow c'}\end{aligned}$$

$$\begin{aligned}\text{ESA} = \omega_2 \sum_{rbb'} \mu_{rb} \mu_{b'r} \tilde{\rho}_{bb'}(\tau) e^{-i\omega_{bb'}\tau - (\omega_{bb'}\tau_2)^2/4} \times \\ \int_0^\infty dt e^{-t^2/4\tau_2^2 + i\omega_{bb'}t/2} \{ e^{-i(\omega_{br} + \omega_2)t - R_{bbr}t} + c.c. \}_{b \rightarrow b'}\end{aligned}$$

where time-dependent amplitudes of the excited- and ground-state wave packets are given by

$$\begin{aligned}\dot{\tilde{\rho}}_{bb'} &= - \sum_{b''b'''} R_{bb'b''b'''} \tilde{\rho}_{b''b'''} \\ \dot{\tilde{\rho}}_{cc'} &= - \sum_{b''b'''} R_{cc'c''c'''} \tilde{\rho}_{c''c'''}\end{aligned}$$

with the initial conditions

$$\begin{aligned}\tilde{\rho}_{bb'}(\tau=0) &= e^{-(\omega_{bb'}\tau_1)^2/4} \sum_c \mu_{bo} \mu_{cb'} \times \\ \int_0^\infty dt e^{-t^2/4\tau_1^2 + i\omega_{bb'}t/2} \{ P_c e^{-i(\omega_{bc} - \omega_1)t - R_{bcb}t} + c.c. \}_{b \rightarrow b'} \\ \tilde{\rho}_{cc'}(\tau=0) &= e^{-(\omega_{cc'}\tau_1)^2/4} \sum_b \mu_{cb} \mu_{bc'} \times \\ \int_0^\infty dt e^{-t^2/4\tau_1^2 + i\omega_{cc'}t/2} \{ P_c e^{i(\omega_{bc} - \omega_1)t - R_{bcc}t} + c.c. \}_{c \rightarrow c'}\end{aligned}$$

Here we neglected the off-diagonal $R_{bcb'c'}$ and $R_{b'rb'r'}$ terms responsible for a transfer of the ground to one-exciton and one- to two-exciton coherences. Notice that this solution is formally equivalent to the doorway–window representation of exciton-vibrational relaxation³⁶ obtained for a decoupled electronic and vibrational coordinates. But now we are working in the basis of mixed exciton-vibrational eigenstates.

Pulses Shorter than Electronic Dephasing (Impulsive Limit). We further suppose that pump and probe pulses are shorter than the decay of the ground to one-exciton and one- to two-exciton coherences (i.e., pulse spectrum is broader than the vibronic line width given by $R_{bcb'e}$ and $R_{b'rb'r'}$). In this case, we get more compact expressions for SE and ESA

$$SE = -2\pi^{1/2}\omega_2\tau_2 \sum_{cbb'} \mu_{cb}\mu_{b'c}\tilde{\rho}_{bb'}(\tau) e^{-i\omega_{bb'}\tau - (\omega_{bb'}\tau_2)^2/4} \times \\ \exp\left\{-\tau_2^2\left(\frac{\epsilon_b + \epsilon_{b'}}{2} - \epsilon_c - \omega_2\right)^2\right\}$$

$$ESA = 2\pi^{1/2}\omega_2\tau_2 \sum_{rbb'} \mu_{rb}\mu_{b'r}\tilde{\rho}_{bb'}(\tau) e^{-i\omega_{bb'}\tau - (\omega_{bb'}\tau_2)^2/4} \times \\ \exp\left\{-\tau_2^2\left(\frac{\epsilon_b + \epsilon_{b'}}{2} - \epsilon_r + \omega_2\right)^2\right\}$$

with the initial conditions

$$\tilde{\rho}_{bb'}(\tau=0) = 2\pi^{1/2}\tau_1 e^{-i\omega_{bb'}\tau_1} \sum_c \mu_{cb}\mu_{b'c}P_c \times \\ \exp\left\{-\tau_1^2\left(\frac{\epsilon_b + \epsilon_{b'}}{2} - \epsilon_c - \omega_1\right)^2\right\}$$

The Redfield Relaxation Tensor. The system-bath interaction in the site representation is taken to be

$$V_{\text{sys-bath}} = V_g + V_e + V_f$$

$$V_g = |g\rangle[f_g^x(x - \Delta_g^x) + f_g^y(y - \Delta_g^y)]\langle g|$$

$$V_e = |e_1\rangle[f_{e_1}^x(x - \Delta_{e_1}^x) + f_{e_1}^y(y - \Delta_{e_1}^y) + F_{e_1}]\langle e_1| + |e_2\rangle[f_{e_2}^x(x - \Delta_{e_2}^x) + f_{e_2}^y(y - \Delta_{e_2}^y) + F_{e_2}]\langle e_2|$$

$$V_f = |f\rangle[f_f^x(x - \Delta_f^x) + f_f^y(y - \Delta_f^y) + F_f]\langle f|$$

$$x = \frac{1}{2^{1/2}}(\beta_x + \beta_x^+) \quad y = \frac{1}{2^{1/2}}(\beta_y + \beta_y^+)$$

where f_g , f_{e2} , f_{e1} , and f_f are bath-induced fluctuations responsible for vibrational relaxation of the x or y coordinate in the corresponding electronic (diabatic) states. The coupling is linear in the vibrational coordinate x or y measured from the minimum of the potential surface. The amplitudes F_{e2} , F_{e1} , and F_f are responsible for electronic relaxation. Notice that we neglect the off-diagonal coupling, i.e., bath-induced modulation of interaction energy M . We suppose that fluctuations acting on different sites and different system coordinates (electronic and two vibrational ones) are uncorrelated. By use of the interaction Hamiltonian, the Redfield tensor can be calculated by a standard way.^{37,38} For example, in the impulsive limit, we need only the one-exciton part $R_{b_1b_2b_3b_4}$ that can be expressed through V_e and the C^e eigenfunctions

$$V_{bb'} = [(C^e)^+ V_e C^e]_{bb'}$$

$$R_{b_1b_2b_3b_4} = -\overline{V_{b_4b_2}V_{b_1b_3}}(J_{b_2b_4} + J_{b_1b_3}) + \\ \delta_{b_2b_4} \sum_b \overline{V_{b_1b}V_{bb_3}}J_{bb_3} + \delta_{b_1b_3} \sum_b \overline{V_{b_4b}V_{bb_2}}J_{bb_4}$$

Here fluctuation amplitudes (Hamiltonian V_e) are transformed to the eigenstate representation. Underlining means an averaging over the bath. The spectral density of system-bath coupling J can be calculated with an arbitrary time scale and correlation matrix of the bath.^{39,40} The simplest (frequency-independent) spectral density of the system-bath coupling is^{7,41}

$$J_{bb'} = \tau_c(1 + \exp(\omega_{bb'}/k_B T))^{-1}$$

where $k_B T$ is the temperature in the units of energy and τ_c is the bath relaxation time.

The Redfield tensor $R_{\alpha\beta}$ in the Liouville space ($\alpha = b_1 + (b_2 - 1)N_b$ and $\beta = b_3 + (b_4 - 1)N_b$) can be expressed as a product $\mathbf{B} \otimes \mathbf{A}$ of the tensors $\mathbf{B}_{b_2b_4}$ and $\mathbf{A}_{b_1b_3}$. We then write down the Redfield tensor in matrix notations

$$R = \sum_n -\overline{(f_{en}^x)^2}(\mathbf{B}_n^x \otimes \mathbf{A}_n^x + \mathbf{A}_n^x \otimes \mathbf{B}_n^x) - \overline{(f_{en}^y)^2}(\mathbf{B}_n^y \otimes \mathbf{A}_n^y + \mathbf{A}_n^y \otimes \mathbf{B}_n^y) - \overline{(F_{en})^2}(\mathbf{B}_n^e \otimes \mathbf{A}_n^e + \mathbf{A}_n^e \otimes \mathbf{B}_n^e) + \\ \mathbf{B}_n \otimes I + I \otimes \mathbf{B}_n$$

$$\mathbf{B}_n^e = C_n^+ C_n \quad \mathbf{A}_n^e = \mathbf{B}_n^{e*} J \quad C_n = \sum_{a,b} |a_x a_y\rangle C_{na,b} \langle b|$$

$$\mathbf{B}_n^x = C_n^+ Q_n^x C_n \quad \mathbf{A}_n^x = \mathbf{B}_n^{x*} J \quad Q_n^x = x - \Delta_{en}^x$$

$$\mathbf{B}_n^y = C_n^+ Q_n^y C_n \quad \mathbf{A}_n^y = \mathbf{B}_n^{y*} J \quad Q_n^y = y - \Delta_{en}^y$$

$$\mathbf{B}_n = \overline{(F_{en})^2} C_n^+ C_n (C_n^+ C_n^* J) + \\ \overline{(f_{en}^x)^2} C_n^+ Q_n^x C_n (C_n^+ Q_n^x C_n^* J) + \\ \overline{(f_{en}^y)^2} C_n^+ Q_n^y C_n (C_n^+ Q_n^y C_n^* J)$$

where I is a δ operator $\delta_{a_x a_y, a'_x a'_y}$, C_n is a fragment of the C^e corresponding to a fixed electronic site n (the sum of independent contributions from different sites appears since we use an uncorrelated disorder model). In terms such as $C_n Q_n C_n$, we assume a matrix multiply, $\mathbf{B}^* J$ denote an array multiply (product of the elements of the matrixes), \otimes stands for a Kronecker tensor product. Such a form is useful for numerical evaluation of the Redfield tensor.

Dynamics of the Excited-State Wave Packet. The wave packet in the nuclear $\{xy\}$ space is given by

$$\Psi(x,y,\tau) = \sum_{bb'} \Psi_b(x,y) \Psi_{b'}(x,y) \tilde{\rho}_{bb'}(\tau) e^{-i\omega_{bb'}\tau}$$

$$\Psi_b(x,y) = \sum_{n,a=\{a_x a_y\}} \varphi_{a_x}(x) \varphi_{a_y}(y) C_{nab}^e$$

where φ are unshifted wave functions of two-dimensional harmonic oscillator.

References and Notes

- (1) Shuvalov, V. A. *Primary light energy conversion in reaction centers of photosynthesis (in Russian)*; Nauka: Moscow, 2000.
- (2) Fleming, G. R.; van Grondelle, R. *Phys. Today* **1994**, 47, 48.
- (3) DeVault D. *Q. Rev. Biophys.* **1980**, 13, 387.
- (4) Warshel, A.; Parson, W. W. *Q. Rev. Biophys.* **2001**, 34, 563.
- (5) Shuvalov, V. A.; Yakovlev, A. G. *FEBS Lett.* **2003**, 540, 26.

- (6) Chernyak, V.; Mukamel, S. *J. Chem. Phys.* **1996**, *105*, 4565.
- (7) Jean, J. M.; Fleming, G. R. *J. Chem. Phys.* **1995**, *103*, 2092.
- (8) Ando, K.; Sumi, H. *J. Phys. Chem. B* **1998**, *102*, 10991.
- (9) Cherepanov, D. A.; Krishtalik, L. I.; Mulikdjanian, A. Y. *Biophys. J.* **2001**, *80*, 1033.
- (10) Vos, M. H.; Rappaport, F.; Lambry, J.-Ch.; Breton, J.; Martin, J.-L. *Nature* **1993**, *363*, 320.
- (11) Vos, M.; Jones, M. R.; Hunter, C. N.; Breton, J.; Lambry, J.-Ch.; Martin, J.-L. *Biochemistry* **1994**, *33*, 6750.
- (12) Vos, M.; Jones, M. R.; Hunter, C. N.; Breton, J.; Martin, J.-L. *Proc. Natl. Acad. Sci. U. S. A.* **1994**, *91*, 12701.
- (13) Vos, M.; Breton, J.; Martin, J.-L. *J. Phys. Chem. B* **1997**, *101*, 9820.
- (14) Vos, M.; Jones, M. R.; Martin, J.-L. *Chem. Phys.* **1998**, *233*, 179.
- (15) Streltsov, A. M.; Yakovlev, A. G.; Shkuropatov, A. Ya.; Shuvalov, V. A. *FEBS Lett.* **1996**, *383*, 129.
- (16) Streltsov, A. M.; Vulto, S. I. E.; Shkuropatov, A. Ya.; Hoff, A. J.; Aartsma, T. J.; Shuvalov, V. A. *J. Phys. Chem. B* **1998**, *102*, 7293.
- (17) Arnett, D. C.; Moser, C. C.; Dutton, P. L.; Scherer, N. F. *J. Phys. Chem. B* **1999**, *103*, 2014.
- (18) Streltsov, A. M.; Aartsma, T. J.; Hoff, A. J.; Shuvalov, V. A. *Phys. Chem. Lett.* **1997**, *266*, 347.
- (19) Vos, M.; Rischel, C.; Jones, M. R.; Martin, J.-L. *Biochemistry* **2000**, *39*, 8353.
- (20) Spörlein, S.; Zinth, W.; Wachtveitl, J. *J. Phys. Chem. B* **1998**, *102*, 7492.
- (21) Yakovlev, A. G.; Shuvalov, V. A. *J. Chin. Chem. Soc.* **2000**, *47*, 709.
- (22) Yakovlev, A. G.; Shkuropatov, A. Ya.; Shuvalov, V. A. *FEBS Lett.* **2000**, *466*, 209.
- (23) Yakovlev, A. G.; Shkuropatov, A. Ya.; Shuvalov, V. A. *Biochemistry* **2002**, *41*, 2667.
- (24) Yakovlev, A. G.; Shkuropatov, A. Ya.; Shuvalov, V. A. *Biochemistry* **2002**, *41*, 14019.
- (25) Gu, X.; Hayashi, M.; Suzuki, S.; Lin, S. H. *Biochim. Biophys. Acta* **1995**, *1229*, 215.
- (26) Lin, S. H.; Hayashi, M.; Suzuki, S.; Gu, X.; Xiao, W.; Sugawara, M. *Chem. Phys.* **1995**, *197*, 435.
- (27) Leegwater, J. A. *J. Phys. Chem.* **1995**, *99*, 11605.
- (28) Jean, J. M.; Friesner, R. A.; Fleming, G. R. *J. Chem. Phys.* **1992**, *96*, 5827.
- (29) Jean, J. M. *J. Chem. Phys.* **1994**, *101*, 10464.
- (30) Zhang, W. M.; Meier, T.; Chernyak, V.; Mukamel, S. *J. Chem. Phys.* **1998**, *108*, 7763.
- (31) Sim, E.; Makri, N. *J. Phys. Chem. B* **1997**, *101*, 5446.
- (32) Sumi, H. *J. Electroanal. Chem.* **1997**, *438*, 11.
- (33) Cherepy, N. J.; Shreve, A. P.; Moore, L. J.; Franzen, S.; Boxer, S. G.; Mathies, R. A. *J. Phys. Chem.* **1994**, *98*, 6023.
- (34) Shuvalov, V. A.; Klevanik, A. V.; Ganago, A. O.; Shkuropatov, A. Ya.; Gubanov, V. S. *FEBS Lett.* **1988**, *237*, 57.
- (35) Mukamel, S. *Principles of nonlinear optical spectroscopy*; Oxford University Press: New York, 1995.
- (36) Novoderezhkin, V.; Monshouwer, R.; van Grondelle, R. *J. Phys. Chem. B* **2000**, *104*, 12056.
- (37) Redfield, A. G. *Adv. Mag. Res.* **1965**, *1*, 1.
- (38) Pollard, W. T.; Felts, A. K.; Friesner, R. A. *Adv. Chem. Phys.* **1996**, *93*, 77.
- (39) Chernyak, V.; Minami, T.; Mukamel, S. *J. Chem. Phys.* **2000**, *112*, 7953.
- (40) Dahlbom, M.; Minami, T.; Chernyak, V.; Pullerits, T.; Sundström, V.; Mukamel, S. *J. Phys. Chem. B* **2000**, *104*, 3976.
- (41) Renger, Th.; May, V.; Kühn, O. *Phys. Rep.* **2001**, *343*, 137.